

# Investigating the Role of Quantum Entanglement in Heavy Ion Collisions through Elliptic Flow

Mira Varma\* and Oliver Baker

*Department of Physics, Yale University, New Haven, CT 06520*

(Dated: June 17, 2024)

This paper investigates the relationship between initial spatial anisotropy and final state momentum anisotropy in heavy ion collisions through the analysis of elliptic flow ( $\nu_2$ ) as a function of transverse momentum ( $p_T$ ). Building upon previous studies on thermalization in heavy ion collisions using transverse momentum distributions, we extend the analysis to the  $p_T$  dependence of  $\nu_2$  in Pb-Pb and Xe-Xe collisions. By employing a two-component model to extract the thermal and hard scattering contributions to the elliptic flow, we aim to gain further insights into the role of quantum entanglement in the rapid thermalization and collective behavior of the quark-gluon plasma (QGP).

## I. INTRODUCTION

Heavy ion collisions (HICs) have emerged as a powerful tool for investigating matter under extreme conditions, akin to those that existed microseconds after the Big Bang [1, 2]. These collisions generate a hot, dense medium known as the quark-gluon plasma (QGP), in which quarks and gluons are momentarily liberated from their hadronic confinement [3]. Studying the QGP is crucial for deepening our understanding of the strong interaction, a fundamental force described by the Standard Model of particle physics. HICs are particularly valuable for exploring critical phenomena, such as the phase transitions from QGP back to hadronic matter, which involve mechanisms like chiral symmetry restoration and color confinement [4, 5]. These phase transitions are significant not only for their role in the early universe but also potentially in the cores of dense neutron stars [6, 7].

The elliptic flow, represented by the symbol  $\nu_2$ , is a key observable that quantifies the anisotropic momentum distribution of particles in the transverse plane, perpendicular to the collision beam direction [8, 9]. It arises from the initial spatial anisotropy of the overlap region in non-central collisions, which creates an almond-shaped interaction volume. The pressure gradients in this asymmetric zone result in greater particle acceleration and emission along the shorter axis, effectively converting the initial spatial anisotropy into a final-state momentum anisotropy [10, 11]. Measuring  $\nu_2$  is essential for understanding the collective behavior and transport properties of the QGP. The magnitude of  $\nu_2$  provides valuable insights into the early stages of the collision, the equation of state of the QGP, and the degree of thermalization attained [12]. By studying  $\nu_2$  as a function of transverse momentum ( $p_T$ ), centrality, and particle species, one can unravel the hydrodynamic behavior of the QGP and the underlying mechanisms of particle production in HICs [13].

Mathematically, elliptic flow can be expressed as the second Fourier coefficient of the particle distribution in azimuthal angle  $\phi$  relative to the reaction plane angle  $\Psi_{RP}$  [9]:

$$\nu_2 = \langle \cos[2(\phi - \Psi_{RP})] \rangle \quad (1)$$

where the brackets  $\langle \dots \rangle$  denote an average over all particles in an event and then over all events. The reaction plane is defined by the beam direction and the impact parameter vector between the colliding nuclei. In practice, the reaction plane is not directly measurable, and the event plane method is commonly employed to estimate  $\nu_2$  [14]:

$$\nu_2\{EP\} = \frac{\langle \cos[2(\phi - \Psi_{EP})] \rangle}{\text{Res}(\Psi_{EP})} \quad (2)$$

where  $\Psi_{EP}$  is the event plane angle determined from the anisotropic flow itself, and  $\text{Res}(\Psi_{EP})$  is the event plane resolution correction factor, which accounts for the difference between the true reaction plane and the measured event plane.

The sequence of events in a heavy ion collision starts with the initial collision, where two relativistic heavy ions collide, creating an overlap region and a non-overlap region [15]. The energy density in the overlap region is so extreme that it overcomes the confining forces between quarks and gluons, leading to the formation of the QGP. As the QGP reaches a high energy density, the quarks and gluons within become deconfined [16].

Remarkably, the QGP undergoes thermalization much faster than predicted by traditional kinetic theories [17]. This rapid equilibration is crucial for the uniform behavior of the plasma during the subsequent hydrodynamic expansion. As the plasma expands, it cools while maintaining thermal equilibrium, responding sensitively to the initial geometric anisotropies of the collision—phenomena that are probed through measurements of elliptic flow [18].

As the cooling progresses, quarks and gluons recombine into hadrons, a process known as hadronization, signaling the transition from the quark-gluon phase back to hadronic matter [19]. After hadronization, the system

---

\* mira.varma@yale.edu

experiences chemical freeze-out, where the temperature drops to a point at which inelastic collisions cease, fixing the ratios of different hadron species [20]. This is closely followed by kinetic freeze-out, where even elastic collisions stop, finalizing the momentum distributions of the particles [21]. Fig. 1 presents a concise overview of this process.

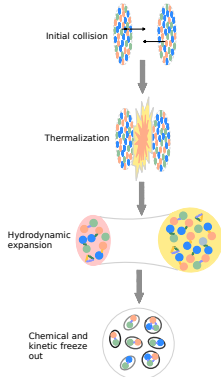


FIG. 1: Timeline of key stages in a heavy ion collision. The process begins with the initial collision and formation of the quark-gluon plasma (QGP), followed by rapid thermalization, hydrodynamic expansion, and phase transitions back to hadronic matter. The timeline highlights the critical events leading to chemical and kinetic freeze-out, marking the system’s evolution from QGP to final-state particles. Figure is adapted from Refs. [22–24].

Recent studies have proposed that the rapid thermalization observed in the QGP may be significantly influenced by quantum mechanical effects, particularly quantum entanglement among the partons (quarks and gluons) in the initial state of the collision [25–27]. This concept of “quantum thermalization through entanglement” suggests that the entangled partonic state can give rise to thermal-like features in the particle distributions immediately after the collision, circumventing the need for multiple scattering events traditionally required for thermalization [25]. Hence, understanding these quantum effects is not only pivotal for explaining the behavior observed in HICs but also for connecting these observations to fundamental quantum field theory.

The thermalization of charged particles in proton-proton (p-p) and lead-lead (Pb-Pb) collisions has been previously attributed to the quantum entanglement of the initial state partons. In [28], the authors demonstrate this by fitting the transverse momentum distributions of these collisions with a combination of exponential functions (thermal component) and power-law functions (hard component), thereby extracting the effective temperatures of the system.

In the present work, we extend this analysis to the  $p_T$  dependence of elliptic flow ( $\nu_2$ ) in both Pb+Pb and Xe+Xe collisions. By examining the elliptic flow, we aim

to gain further insights into the collective behavior of the system and the underlying mechanisms driving the observed anisotropies. This study is not only a continuation but also an expansion of the previous research, emphasizing the significance of quantum entanglement in shaping the outcomes of heavy ion collisions.

It is important to note that the data used in this study for Pb+Pb collisions at  $\sqrt{s_{NN}} = 2.76$  TeV and  $\sqrt{s_{NN}} = 5.02$  TeV, as well as for Xe+Xe collisions at  $\sqrt{s_{NN}} = 5.44$  TeV, were obtained using different methods. The ALICE collaboration employed the event plane method with a pseudorapidity gap of  $|\Delta\eta| > 2.0$  for the Xe+Xe collisions at  $\sqrt{s_{NN}} = 5.44$  TeV [29] and the Pb-Pb collisions at  $\sqrt{s_{NN}} = 2.76$  TeV [30]. In contrast, the ATLAS collaboration used the scalar product method for the Pb+Pb collisions at  $\sqrt{s_{NN}} = 5.02$  TeV [31]. These differences in data-taking methods may influence the observed centrality dependence of the hard scattering ratio and should be considered when interpreting the results.

## II. THE TWO-COMPONENT MODEL

In this study, we analyze the  $\nu_2$  data from Xe+Xe collisions at  $\sqrt{s_{NN}} = 5.44$  TeV and Pb+Pb collisions at  $\sqrt{s_{NN}} = 5.02$  TeV and 2.76 TeV, measured by the ALICE and ATLAS collaborations [29–31]. Since the transverse momentum ( $p_T$ ) is much smaller than the longitudinal momenta along the beam direction, the  $\nu_2$  vs  $p_T$  dependence can be approximated as [32]:

$$\frac{d\nu_2(p_T)}{dp_T} \approx \frac{\nu_2}{\langle p_T \rangle} \quad (3)$$

We employ a two-component model to describe  $\nu_2$  as a function of transverse momentum ( $p_T$ ), which allows us to extract the thermal and hard scattering contributions to the elliptic flow [33, 34].

The thermal contribution is given by:

$$\frac{\nu_2}{p_T}(\text{thermal}) = A_{\text{th}} \cdot \exp\left(-\frac{m_T}{T_{\text{th}}}\right) \quad (4)$$

where  $A_{\text{th}}$  and  $T_{\text{th}}$  are fitting parameters, and  $m_T$  is the transverse mass defined as:

$$m_T = \sqrt{m^2 + p_T^2} \quad (5)$$

In Equation 5, we use the pion mass, which does not have a sensitive effect on the data.

The hard scattering contribution is given by:

$$\frac{\nu_2}{p_T}(\text{hard}) = \frac{A_{\text{hard}}}{\left(1 + \frac{m_T^2}{T^{2n}}\right)^n} \quad (6)$$

where  $A_{\text{hard}}$ ,  $T$ , and  $n$  are fitting parameters, and  $m_T$  is defined as in Equation 5.

Our two-component model is the sum of the thermal and hard scattering contributions, as described by Equations 4 and 6.

The fits are performed using Python's SciPy package, and the quality of the fits is assessed using  $R^2$  (the goodness of fit) and  $\chi^2$  values. The ratio of the hard scattering integral to the total fit integral is calculated for each process to quantify the relative contribution of the hard processes to the elliptic flow. The fit parameters, along with their uncertainties, are included in the appendix.

### III. RESULTS AND DISCUSSION

#### A. Overview of the main findings

The analysis of the elliptic flow ( $v_2$ ) as a function of transverse momentum ( $p_T$ ) in Xe+Xe collisions at  $\sqrt{s_{NN}} = 5.44$  TeV and Pb+Pb collisions at  $\sqrt{s_{NN}} = 5.02$  TeV and 2.76 TeV reveals a complex interplay between thermal and hard scattering processes contributing to the observed anisotropy. The two-component model, which combines thermal and hard scattering contributions, successfully describes the  $v_2(p_T)$  data across various centrality classes in all three collision systems. The ratio of the hard scattering integral to the total fit integral exhibits non-monotonic behavior with centrality in both  $\sqrt{s_{NN}} = 5.44$  TeV and Pb+Pb collisions at  $\sqrt{s_{NN}} = 5.02$ , while a monotonic increase is seen in Pb+Pb collisions at  $\sqrt{s_{NN}} = 2.76$  TeV. This indicates a sensitivity to the collision conditions.

In all systems and centralities studied, the thermal component dominates at low  $p_T$  ( $p_T \lesssim 2$  GeV/c), while the hard scattering component becomes more significant at higher  $p_T$ . This suggests that the thermal component arises from the collective behavior of the QGP, which is more pronounced at lower  $p_T$ . The hard scattering component, on the other hand, reflects initial state anisotropies and jet-like correlations, which are more significant at higher  $p_T$ . The non-monotonic behavior of the hard scattering ratio with centrality suggests that the balance between thermal and hard scattering components is sensitive to the collision geometry, QGP size, and collision energy. This trend is observed in both Xe+Xe and Pb+Pb ( $\sqrt{s_{NN}} = 5.02$ ) collisions, indicating it is a general feature of elliptic flow in heavy ion collisions.

Centrality	$\frac{\text{hard scattering integral}}{\text{total integral}}$	$R^2$	$\chi^2$
20-30%	$0.56 \pm 0.01$	0.9959	8.86e-06
30-40%	$0.56 \pm 0.01$	0.9952	1.24e-05
40-50%	$0.44 \pm 0.01$	0.9954	1.17e-05

TABLE I: Ratios of hard scattering integral to total fit integral for ALICE Xe+Xe collisions at  $\sqrt{s_{NN}} = 5.44$  TeV, with a pseudorapidity coverage of  $|\eta| < 0.8$ .

Centrality	$\frac{\text{hard scattering integral}}{\text{total integral}}$	$R^2$	$\chi^2$
20-30%	$0.44 \pm 0.01$	0.9952	6.71e-06
30-40%	$0.60 \pm 0.01$	0.9700	5.83e-06
40-50%	$0.50 \pm 0.01$	0.9981	4.87e-06

TABLE II: Ratios of hard scattering integral to total fit integral for ATLAS Pb+Pb collisions at  $\sqrt{s_{NN}} = 5.02$  TeV, with a pseudorapidity coverage of  $|\eta| < 2.5$ .

Centrality	$\frac{\text{hard scattering integral}}{\text{total integral}}$	$R^2$	$\chi^2$
20-30%	$0.49 \pm 0.01$	0.9976	5.76e-6
30-40%	$0.51 \pm 0.01$	0.9921	2.15e-05
40-50%	$0.61 \pm 0.01$	0.9914	3.52e-05

TABLE III: Ratios of hard scattering integral to total fit integral for ALICE Pb+Pb collisions at  $\sqrt{s_{NN}} = 2.76$  TeV, with a pseudorapidity coverage of  $|\eta| < 0.8$ .

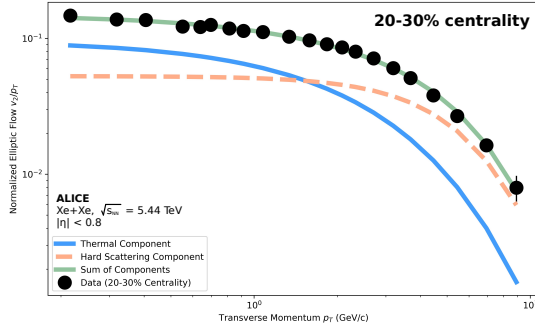
#### B. Xe+Xe collisions at $\sqrt{s_{NN}} = 5.44$ TeV

Xe+Xe collisions at  $\sqrt{s_{NN}} = 5.44$  TeV are studied for the 20-30%, 30-40%, and 40-50% centrality classes (Figure 2). The two-component model provides a good description of the data in all classes, with high  $R^2$  and low  $\chi^2$  values (Table 1). The thermal component dominates at low  $p_T$ , transitioning to the hard scattering component at higher  $p_T$  ( $\sim 2-3$  GeV/c), depending on centrality. The ratio of the hard scattering integral to the total fit integral shows non-monotonic behavior with centrality, remaining constant between 20-30% and 30-40% centrality ( $0.56 \pm 0.01$ ) and decreasing at 40-50% ( $0.44 \pm 0.01$ ). At low  $p_T$  ( $< 1$  GeV/c),  $v_2$  is similar across centralities, indicating consistent collective QGP behavior. This similarity is expected from a theoretical perspective, as the low  $p_T$  region is dominated by the collective expansion of the QGP, which is less sensitive to the initial state geometry [35], [36].

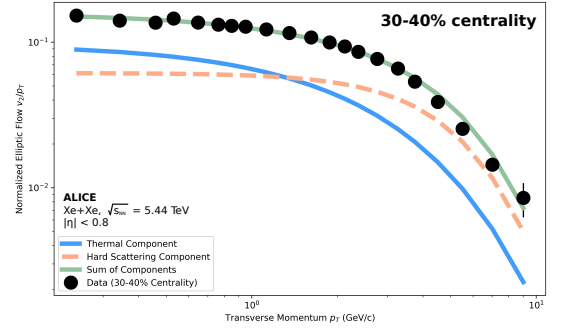
#### C. Pb+Pb collisions at $\sqrt{s_{NN}} = 5.02$ TeV and 2.76 TeV

The  $v_2(p_T)$  in Pb+Pb collisions is studied at  $\sqrt{s_{NN}} = 5.02$  TeV and 2.76 TeV for the 20-30%, 30-40%, and 40-50% centrality classes (Figures 3 and 4). The two-component model accurately describes the data at both energies, with high  $R^2$  values and low  $\chi^2$  values (Tables 2 and 3). The thermal component dominates at low  $p_T$ , transitioning to the hard scattering component at higher  $p_T$ .

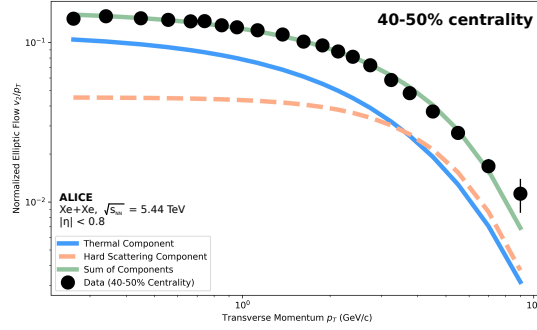
Comparing results between the two energies,  $v_2$  is generally larger at  $\sqrt{s_{NN}} = 5.02$  TeV, particularly at higher  $p_T$ , likely due to higher energy density and larger QGP volume. The behavior of the hard scattering ratio across centrality classes is similar for both collision energies,



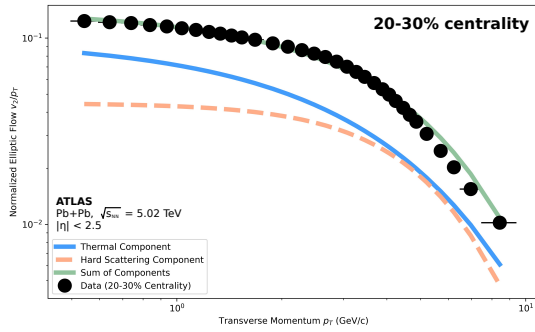
(a) 20-30% centrality



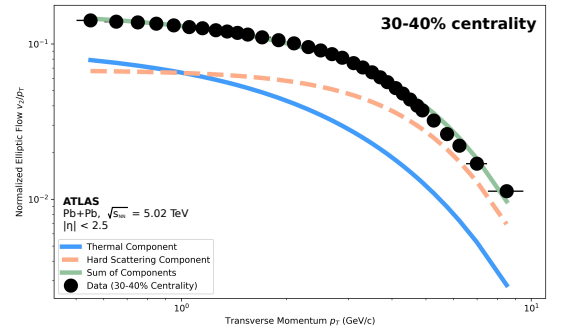
(b) 30-40% centrality



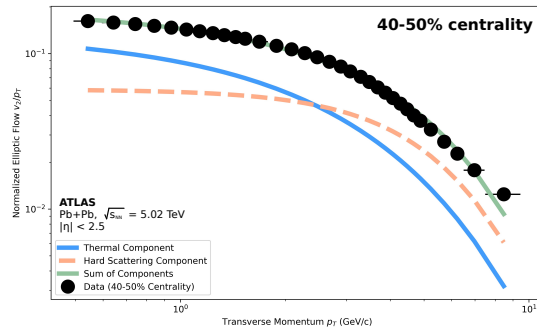
(c) 40-50% centrality

FIG. 2: Elliptic flow  $\nu_2$  vs  $p_T$  for Xe+Xe collisions at  $\sqrt{s_{NN}} = 5.44$  TeV at various centralities. Data is from [29].

(a) 20-30% centrality

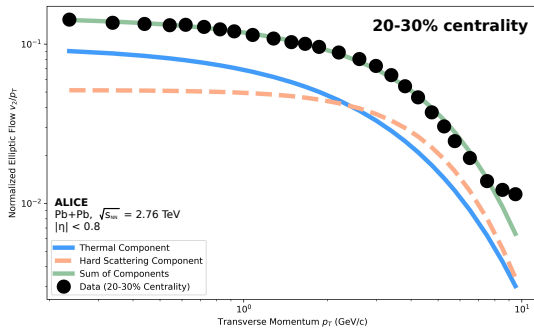


(b) 30-40% centrality

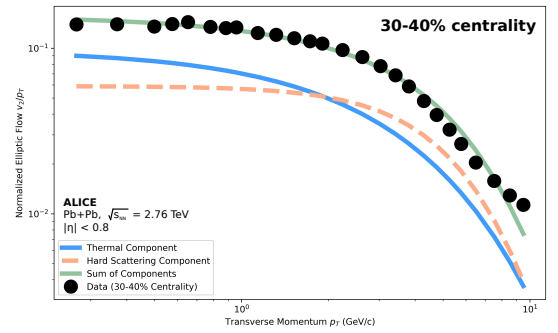


(c) 40-50% centrality

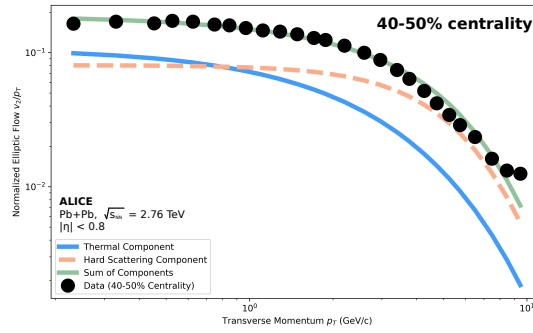
FIG. 3: Elliptic flow  $\nu_2$  vs  $p_T$  for Pb+Pb collisions at  $\sqrt{s_{NN}} = 5.02$  TeV at various centralities. Data is from [31].



(a) 20-30% centrality



(b) 30-40% centrality



(c) 40-50% centrality

FIG. 4: Elliptic flow  $\nu_2$  vs  $p_T$  for Pb+Pb collisions at  $\sqrt{s_{NN}} = 2.76$  TeV at various centralities. All error bars are smaller than the data points. Data is from [30].

with a net increase from 20-30% to 40-50% centrality. However, the highest ratio value is observed in the 30-40% centrality class for both  $\sqrt{s_{NN}} = 5.02$  TeV ( $0.60 \pm 0.01$ ). At  $\sqrt{s_{NN}} = 5.02$  TeV, the hard scattering ratio is lowest at 20-30% ( $0.44 \pm 0.01$ ), and the 40-50% centrality class falls in between ( $0.50 \pm 0.01$ ). For  $\sqrt{s_{NN}} = 2.76$  TeV, the ratio increases monotonically with centrality, with the lowest value at 20-30% ( $0.49 \pm 0.01$ ), followed 30-40% ( $0.51 \pm 0.01$ ), and the highest value at 40-50% centrality ( $0.61 \pm 0.01$ ).

It is important to note that the ATLAS measurement at 5.02 TeV has a wider pseudorapidity coverage ( $|\eta| < 2.5$ ) compared to the ALICE measurements at 2.76 TeV ( $|\eta| < 0.8$ ). This difference in pseudorapidity coverage may influence the observed centrality dependence of the hard scattering ratio, as  $v_2$  typically decreases towards forward and backward rapidities [37]. Additionally, the relative contributions of the thermal and hard scattering processes to the elliptic flow may vary with pseudorapidity [38], which can affect the extracted fit parameters and their centrality dependence.

Another crucial factor to consider is the difference in the data-taking methods employed by the ALICE and ATLAS collaborations. The ALICE collaboration used the event plane method with a pseudorapidity gap of  $|\Delta\eta| > 2.0$  for the Pb+Pb collisions at  $\sqrt{s_{NN}} = 2.76$  TeV and the Xe+Xe collisions at  $\sqrt{s_{NN}} = 5.44$ , while the ATLAS collaboration used the scalar product method for the Pb+Pb collisions at  $\sqrt{s_{NN}} = 5.02$ . Although both methods aim to suppress non-flow effects, the different techniques may lead to variations in the extracted  $v_2$  values and, consequently, the centrality dependence of the hard scattering ratio. Future studies using consistent data-taking methods across different collision systems and energies would help to disentangle the effects of the experimental techniques from the underlying physics.

#### D. Interpretation and Implications

The non-monotonic behavior of the hard scattering ratio with centrality suggests that the relative contributions of hard and thermal processes to the elliptic flow are sensitive to the collision geometry, QGP size, and collision energy. Potential factors influencing this behavior include the changing shape and size of the initial overlap region, path-length dependent energy loss of hard partons [39, 40], the interplay between soft and hard components of  $v_2$ , and the role of initial state fluctuations.

The centrality dependence of the hard scattering ratio may provide insights into the rapid thermalization and collective behavior of the QGP. The non-monotonic trend suggests that the balance between hard and thermal processes, which contribute to the elliptic flow, varies with the collision centrality. This variation could be related to the different rates of thermalization and the strength of collective effects in the QGP at different centralities [41, 42]. The rapid thermalization of the QGP is believed

to be driven by the strong coupling and quantum entanglement of the system [43], and the collective behavior is a consequence of this thermalization.

The comparison of Xe+Xe and Pb+Pb collisions at different centralities and collision energies reveals distinct patterns in the centrality dependence of the hard scattering ratio. The lowest ratio value is observed in the 40-50% centrality class for Xe+Xe collisions, while for Pb+Pb collisions at  $\sqrt{s_{NN}} = 5.02$  TeV, it is found in the 20-30% centrality class. In contrast, the hard scattering ratio increases monotonically with centrality for Pb+Pb collisions at  $\sqrt{s_{NN}} = 2.76$  TeV. These differences suggest that the interplay between hard and thermal processes in the development of elliptic flow is sensitive to the collision system, energy, and associated geometry [37]. The larger size of the Pb nuclei compared to Xe may lead to a more pronounced impact of the collision geometry on the relative contributions of hard and thermal processes [44, 45].

The differences in the centrality dependence of the hard scattering ratio between Xe+Xe and Pb+Pb collisions also highlight the potential role of system size in the development of collectivity [41, 42]. The smaller size of the Xe+Xe system may lead to a faster expansion and cooling of the QGP, affecting the balance between hard and thermal processes. On the other hand, the larger size of the Pb+Pb system may allow for a more extended period of collectivity, enabling a stronger influence of hard processes on the elliptic flow. This connection between system size and the development of collectivity contributes to our understanding of the scaling properties of flow observables and the transport properties of the QGP.

Our findings, which demonstrate the centrality-dependent contributions of hard and thermal processes to the elliptic flow, provide a new perspective on the interplay between these processes and their connection to the rapid thermalization and collective behavior of the QGP. These results complement previous studies on quantum effects, such as entanglement, in the QGP [25, 46]. By investigating the centrality dependence of the hard scattering ratio, we contribute to a more comprehensive understanding of the role of quantum effects in the development of collective flow and the thermalization of the QGP in heavy ion collisions.

The potential influence of pseudorapidity on the relative contributions of thermal and hard processes to the elliptic flow [38] highlights the importance of considering the experimental conditions when interpreting the results. Future studies with comparable pseudorapidity coverages across different collision systems and energies will further disentangle the effects of collision energy, system size, and pseudorapidity on the thermal and hard scattering components of  $v_2$ . Such studies will help to better understand the connection between the observed centrality dependence of the hard scattering ratio and the underlying quantum effects governing the behavior of the QGP [47].

## IV. CONCLUSION

In this paper, we investigated the role of quantum entanglement in the rapid thermalization and collective behavior of the quark-gluon plasma (QGP) by analyzing the elliptic flow ( $v_2$ ) as a function of transverse momentum ( $p_T$ ) in Pb+Pb and Xe+Xe collisions. Our two-component model successfully extracts the thermal and hard scattering contributions to the elliptic flow, revealing new insights into the underlying mechanisms driving the observed anisotropies.

The key finding is the non-monotonic behavior of the ratio of the hard scattering integral to the total fit integral with centrality, observed in Xe+Xe collisions at  $\sqrt{s_{NN}} = 5.44$  TeV and Pb+Pb collisions at  $\sqrt{s_{NN}} = 5.02$  TeV, while a monotonic increase is seen in Pb+Pb collisions at  $\sqrt{s_{NN}} = 2.76$  TeV. This behavior points to a complex interplay between the hard and thermal processes, sensitive to the collision system, energy, and centrality, and may be connected to the role of quantum entanglement in the QGP's rapid thermalization and collective behavior [25, 43].

Our findings have significant implications for interpreting experimental observations and developing theoretical models of the QGP. The non-monotonic behavior of the thermal and hard process contributions with centrality suggests that the observed elliptic flow depends on the interplay between quantum entanglement effects and specific collision conditions. This insight can guide future experimental data interpretation and help disentangle the contributions of different physical mechanisms to the observed anisotropies. Moreover, our study underscores the importance of incorporating quantum entanglement in models of QGP evolution and thermalization [47, 48], potentially inspiring more sophisticated theoretical frameworks that explicitly account for quantum effects.

The sensitivity of the thermal and hard process contributions to the collision conditions highlights the need for a comprehensive approach in studying the QGP's proper-

ties and dynamics. Future experimental and theoretical studies should carefully consider specific collision parameters when investigating the role of quantum entanglement in heavy ion collisions.

To further advance our understanding, future research should extend the analysis to a wider range of collision systems and energies, incorporate additional observables [49], develop theoretical models that explicitly incorporate quantum entanglement effects, and explore connections between quantum entanglement and other novel phenomena, such as the chiral magnetic effect [50] and hyperon polarization [51].

While our study provides valuable insights, it is important to acknowledge the potential limitations of our approach. The two-component model, although successful in describing the elliptic flow data, is a simplified representation of the complex dynamics in heavy ion collisions. Future research could explore more sophisticated models that incorporate quantum effects more explicitly, such as those based on the AdS/CFT correspondence [52–54] or the color glass condensate framework [55]. Additionally, our analysis focuses on a limited range of collision systems and energies. Extending the study to a wider variety of collision systems, such as proton-nucleus or light ion collisions, and exploring a broader range of energies could provide a more comprehensive understanding of the role of quantum effects in different collision scenarios. Furthermore, the inclusion of additional observables, such as higher-order flow harmonics [56] or event-by-event fluctuations [57], could offer complementary insights into the interplay between quantum entanglement and the collective behavior of the QGP.

## ACKNOWLEDGMENTS

The authors gratefully acknowledge funding support from the Department of Energy Office of Science Award DE-FG02-92ER40704.

### Appendix A: Fit Parameters and Uncertainties

In this appendix, we provide detailed tables of the fit parameters and their uncertainties for the Xe+Xe and Pb+Pb collisions at different energies and centrality classes.

#### 1. ALICE Xe+Xe 5.44 TeV

Centrality	$A_{\text{th}}$	$T_{\text{th}}$	$A_{\text{hard}}$	$T$	$n$
20-30%	$0.1 \pm 2.94 \times 10^{-6}$	$2.157 \pm 7.27 \times 10^{-5}$	$0.0528 \pm 2.99 \times 10^{-6}$	$5.38 \pm 9.91 \times 10^{-5}$	$5.0 \pm 1.43 \times 10^{-3}$
30-40%	$0.1 \pm 4.44 \times 10^{-6}$	$2.376 \pm 1.18 \times 10^{-4}$	$0.0614 \pm 4.49 \times 10^{-6}$	$5.0 \pm 4.77 \times 10^{-5}$	$5.0 \pm 1.12 \times 10^{-3}$
40-50%	$0.118 \pm 8.14 \times 10^{-6}$	$2.487 \pm 1.87 \times 10^{-4}$	$0.0454 \pm 8.21 \times 10^{-6}$	$5.0 \pm 1.04 \times 10^{-4}$	$5.0 \pm 3.43 \times 10^{-3}$

TABLE IV: Fit parameters and uncertainties for ALICE Xe+Xe collisions at  $\sqrt{s_{NN}} = 5.44$  TeV.

## 2. ATLAS Pb+Pb 5.02 TeV

Centrality	$A_{\text{th}}$	$T_{\text{th}}$	$A_{\text{hard}}$	$T$	$n$
20-30%	$0.1 \pm 8.06 \times 10^{-6}$	$3.013 \pm 2.68 \times 10^{-4}$	$0.0448 \pm 8.16 \times 10^{-6}$	$5.0 \pm 7.91 \times 10^{-5}$	$5.0 \pm 2.10 \times 10^{-3}$
30-40%	$0.1 \pm 2.24 \times 10^{-6}$	$2.381 \pm 6.63 \times 10^{-5}$	$0.0678 \pm 2.33 \times 10^{-6}$	$5.0 \pm 8.02 \times 10^{-6}$	$5.0 \pm 2.42 \times 10^{-4}$
40-50%	$0.138 \pm 1.78 \times 10^{-6}$	$2.249 \pm 3.72 \times 10^{-5}$	$0.0589 \pm 1.87 \times 10^{-6}$	$5.0 \pm 1.31 \times 10^{-5}$	$5.0 \pm 2.15 \times 10^{-4}$

TABLE V: Fit parameters and uncertainties for ATLAS Pb+Pb collisions at  $\sqrt{s_{NN}} = 5.02$  TeV.

## 3. ALICE Pb+Pb 2.76 TeV

Centrality	$A_{\text{th}}$	$T_{\text{th}}$	$A_{\text{hard}}$	$T$	$n$
20-30%	$0.1 \pm 3.31 \times 10^{-6}$	$2.712 \pm 1.01 \times 10^{-4}$	$0.0515 \pm 3.35 \times 10^{-6}$	$5.0 \pm 1.17 \times 10^{-5}$	$5.0 \pm 6.00 \times 10^{-4}$
30-40%	$0.1 \pm 5.01 \times 10^{-6}$	$2.871 \pm 1.59 \times 10^{-4}$	$0.0591 \pm 5.06 \times 10^{-6}$	$5.0 \pm 2.55 \times 10^{-5}$	$5.0 \pm 8.98 \times 10^{-4}$
40-50%	$0.111 \pm 2.12 \times 10^{-6}$	$2.312 \pm 5.15 \times 10^{-5}$	$0.0807 \pm 2.16 \times 10^{-6}$	$5.0 \pm 1.41 \times 10^{-5}$	$5.0 \pm 2.54 \times 10^{-4}$

TABLE VI: Fit parameters and uncertainties for ALICE Pb+Pb collisions at  $\sqrt{s_{NN}} = 2.76$  TeV.

- [1] Ulrich Heinz and Raimond Snellings. Collective flow and viscosity in relativistic heavy-ion collisions. *Ann. Rev. Nucl. Part. Sci.*, 63:123–151, 2013.
- [2] Wit Busza, Krishna Rajagopal, and Wilke van der Schee. Heavy Ion Collisions: The Big Picture, and the Big Questions. *Ann. Rev. Nucl. Part. Sci.*, 68:339–376, 2018.
- [3] Edward Shuryak. Strongly coupled quark-gluon plasma in heavy ion collisions. *Rev. Mod. Phys.*, 89:035001, 2017.
- [4] Kenji Fukushima and Tetsuo Hatsuda. The phase diagram of dense QCD. *Rept. Prog. Phys.*, 74:014001, 2011.
- [5] A. Bazavov et al. Chiral crossover in QCD at zero and non-zero chemical potentials. *Phys. Lett. B*, 795:15–21, 2019.
- [6] D. Boyanovsky, H. J. de Vega, and D. J. Schwarz. Phase transitions in the early and the present universe. *Ann. Rev. Nucl. Part. Sci.*, 56:441–500, 2006.
- [7] Fridolin Weber. Strange quark matter and compact stars. *Prog. Part. Nucl. Phys.*, 54:193–288, 2005.
- [8] Jean-Yves Ollitrault. Anisotropy as a signature of transverse collective flow. *Phys. Rev. D*, 46:229–245, 1992.
- [9] S. Voloshin and Y. Zhang. Flow study in relativistic nuclear collisions by Fourier expansion of Azimuthal particle distributions. *Z. Phys. C*, 70:665–672, 1996.
- [10] B. Alver and G. Roland. Collision geometry fluctuations and triangular flow in heavy-ion collisions. *Phys. Rev. C*, 81:054905, 2010. [Erratum: *Phys.Rev.C* 82, 039903 (2010)].
- [11] Derek Teaney and Li Yan. Triangularity and Dipole Asymmetry in Heavy Ion Collisions. *Phys. Rev. C*, 83:064904, 2011.
- [12] Peter F. Kolb and Ulrich W. Heinz. *Hydrodynamic description of ultrarelativistic heavy ion collisions*, pages 634–714. 5 2003.
- [13] B. I. Abelev et al. Systematic Measurements of Identified Particle Spectra in  $pp$ ,  $d^+$  Au and Au+Au Collisions from STAR. *Phys. Rev. C*, 79:034909, 2009.
- [14] Arthur M. Poskanzer and S. A. Voloshin. Methods for analyzing anisotropic flow in relativistic nuclear collisions. *Phys. Rev. C*, 58:1671–1678, 1998.
- [15] Michael L. Miller, Klaus Reyggers, Stephen J. Sanders, and Peter Steinberg. Glauber modeling in high energy nuclear collisions. *Ann. Rev. Nucl. Part. Sci.*, 57:205–243, 2007.
- [16] Miklos Gyulassy and Larry McLerran. New forms of QCD matter discovered at RHIC. *Nucl. Phys. A*, 750:30–63, 2005.
- [17] R. Baier, Alfred H. Mueller, D. Schiff, and D. T. Son. 'Bottom up' thermalization in heavy ion collisions. *Phys. Lett. B*, 502:51–58, 2001.
- [18] D. Teaney, J. Lauret, and Edward V. Shuryak. Flow at the SPS and RHIC as a quark gluon plasma signature. *Phys. Rev. Lett.*, 86:4783–4786, 2001.
- [19] Peter Braun-Munzinger, Volker Koch, Thomas Schäfer, and Johanna Stachel. Properties of hot and dense matter from relativistic heavy ion collisions. *Phys. Rept.*, 621:76–126, 2016.
- [20] Peter Braun-Munzinger, Krzysztof Redlich, and Johanna Stachel. *Particle production in heavy ion collisions*, pages 491–599. 4 2003.
- [21] F. Becattini, M. Gazdzicki, A. Keranen, J. Manninen, and R. Stock. Chemical equilibrium in nucleus nucleus collisions at relativistic energies. *Phys. Rev. C*, 69:024905, 2004.
- [22] A. Bazavov, N. Brambilla, H. T. Ding, P. Petreczky, H. P. Schadler, A. Vairo, and J. H. Weber. Polyakov loop in 2+1 flavor QCD from low to high temperatures. *Phys. Rev. D*, 93(11):114502, 2016.
- [23] Roel Aaij et al. Observation of  $J/\psi p$  Resonances Consistent with Pentaquark States in  $\Lambda_b^0 \rightarrow J/\psi K^- p$  Decays. *Phys. Rev. Lett.*, 115:072001, 2015.

- [24] Charles Gale, Sangyong Jeon, Björn Schenke, Prithwish Tribedy, and Raju Venugopalan. Event-by-event anisotropic flow in heavy-ion collisions from combined Yang-Mills and viscous fluid dynamics. *Phys. Rev. Lett.*, 110(1):012302, 2013.
- [25] Alexander Rothkopf. Heavy Quarkonium in Extreme Conditions. *Phys. Rept.*, 858:1–117, 2020.
- [26] Roel Aaij et al. Centrality determination in heavy-ion collisions with the LHCb detector. *JINST*, 17(05):P05009, 2022.
- [27] R. J. Fries, Berndt Muller, C. Nonaka, and S. A. Bass. Hadronization in heavy ion collisions: Recombination and fragmentation of partons. *Phys. Rev. Lett.*, 90:202303, 2003.
- [28] Arvind Khuntia, Himanshu Sharma, Swatantra Kumar Tiwari, Raghunath Sahoo, and Jean Cleymans. Radial flow and differential freeze-out in proton-proton collisions at  $\sqrt{s} = 7$  TeV at the LHC. *Eur. Phys. J. A*, 55(1):3, 2019.
- [29] S. Acharya et al. Anisotropic flow in Xe-Xe collisions at  $\sqrt{s_{NN}} = 5.44$  TeV. *Phys. Lett. B*, 784:82–95, 2018.
- [30] Betty Abelev et al. Anisotropic flow of charged hadrons, pions and (anti-)protons measured at high transverse momentum in Pb-Pb collisions at  $\sqrt{s_{NN}}=2.76$  TeV. *Phys. Lett. B*, 719:18–28, 2013.
- [31] Morad Aaboud et al. Measurement of the azimuthal anisotropy of charged particles produced in  $\sqrt{s_{NN}} = 5.02$  TeV Pb+Pb collisions with the ATLAS detector. *Eur. Phys. J. C*, 78(12):997, 2018.
- [32] Naomi van der Kolk. *To flow or not to flow: A study of elliptic flow and nonflow in proton-proton collisions in ALICE*. PhD thesis, Utrecht U., 2012.
- [33] Chao Zhang, Liang Zheng, Shusu Shi, and Zi-Wei Lin. Using local nuclear scaling of initial condition parameters to improve the system size dependence of transport model descriptions of nuclear collisions. *Phys. Rev. C*, 104(1):014908, 2021.
- [34] O. K. Baker and D. E. Kharzeev. Thermal radiation and entanglement in proton-proton collisions at energies available at the CERN Large Hadron Collider. *Phys. Rev. D*, 98(5):054007, 2018.
- [35] Huichao Song and Ulrich W. Heinz. Suppression of elliptic flow in a minimally viscous quark-gluon plasma. *Phys. Lett. B*, 658:279–283, 2008.
- [36] Jacquelyn Noronha-Hostler, Jorge Noronha, and Carsten Greiner. Transport Coefficients of Hadronic Matter near  $T(c)$ . *Phys. Rev. Lett.*, 103:172302, 2009.
- [37] S. Voloshin and Y. Zhang. Flow study in relativistic nuclear collisions by Fourier expansion of Azimuthal particle distributions. *Z. Phys. C*, 70:665–672, 1996.
- [38] Arthur M. Poskanzer and S. A. Voloshin. Methods for analyzing anisotropic flow in relativistic nuclear collisions. *Phys. Rev. C*, 58:1671–1678, 1998.
- [39] Karen M. Burke et al. Extracting the jet transport coefficient from jet quenching in high-energy heavy-ion collisions. *Phys. Rev. C*, 90(1):014909, 2014.
- [40] Jorge Casalderrey-Solana, Doga Can Gulhan, José Guilherme Milhano, Daniel Pablos, and Krishna Rajagopal. Towards a hybrid strong/weak coupling approach to jet quenching. *Nucl. Phys. A*, 932:421–425, 2014.
- [41] Bjoern Schenke, Charles Gale, and Sangyong Jeon. MARTINI: An Event generator for relativistic heavy-ion collisions. *Phys. Rev. C*, 80:054913, 2009.
- [42] Jonah E. Bernhard, J. Scott Moreland, and Steffen A. Bass. Bayesian estimation of the specific shear and bulk viscosity of quark-gluon plasma. *Nature Phys.*, 15(11):1113–1117, 2019.
- [43] Aleks Kurkela, Aleksas Mazeliauskas, Jean-François Paquet, Sören Schlichting, and Derek Teaney. Effective kinetic description of event-by-event pre-equilibrium dynamics in high-energy heavy-ion collisions. *Phys. Rev. C*, 99(3):034910, 2019.
- [44] J. Scott Moreland, Jonah E. Bernhard, and Steffen A. Bass. Alternative ansatz to wounded nucleon and binary collision scaling in high-energy nuclear collisions. *Phys. Rev. C*, 92(1):011901, 2015.
- [45] Weiyao Ke, J. Scott Moreland, Jonah E. Bernhard, and Steffen A. Bass. Constraints on rapidity-dependent initial conditions from charged particle pseudorapidity densities and two-particle correlations. *Phys. Rev. C*, 96(4):044912, 2017.
- [46] Jürgen Berges, Stefan Floerchinger, and Raju Venugopalan. Dynamics of entanglement in expanding quantum fields. *JHEP*, 04:145, 2018.
- [47] S. Schlichting and D. Teaney. The first fm/c of heavy-ion collisions. *Annual Review of Nuclear and Particle Science*, 69:447–476, 2019.
- [48] Michal P. Heller and Michal Spalinski. Hydrodynamics Beyond the Gradient Expansion: Resurgence and Resummation. *Phys. Rev. Lett.*, 115(7):072501, 2015.
- [49] Giuliano Giacalone, Fernando G. Gardim, Jacquelyn Noronha-Hostler, and Jean-Yves Ollitrault. Skewness of mean transverse momentum fluctuations in heavy-ion collisions. *Phys. Rev. C*, 103(2):024910, 2021.
- [50] D. E. Kharzeev, J. Liao, S. A. Voloshin, and G. Wang. Chiral magnetic and vortical effects in high-energy nuclear collisions—a status report. *Progress in Particle and Nuclear Physics*, 88:1–28, 2016.
- [51] F. Becattini, M. Buzzegoli, and A. Palermo. Spin-thermal shear coupling in a relativistic fluid. *Phys. Lett. B*, 820:136519, 2021.
- [52] Juan Martin Maldacena. The Large N limit of superconformal field theories and supergravity. *Adv. Theor. Math. Phys.*, 2:231–252, 1998.
- [53] Steven S. Gubser. Breaking an Abelian gauge symmetry near a black hole horizon. *Phys. Rev. D*, 78:065034, 2008.
- [54] Hans Bantilan, Frans Pretorius, and Steven S. Gubser. Simulation of Asymptotically AdS5 Spacetimes with a Generalized Harmonic Evolution Scheme. *Phys. Rev. D*, 85:084038, 2012.
- [55] Francois Gelis, Edmond Iancu, Jamal Jalilian-Marian, and Raju Venugopalan. The Color Glass Condensate. *Ann. Rev. Nucl. Part. Sci.*, 60:463–489, 2010.
- [56] Li Yan and Jean-Yves Ollitrault. Universal fluctuation-driven eccentricities in proton-proton, proton-nucleus and nucleus-nucleus collisions. *Phys. Rev. Lett.*, 112:082301, 2014.
- [57] Giuliano Giacalone, Jacquelyn Noronha-Hostler, and Jean-Yves Ollitrault. Relative flow fluctuations as a probe of initial state fluctuations. *Phys. Rev. C*, 95(5):054910, 2017.